ADVANCED OPTICAL MATERIALS
www.advopticalmat.de

Photoconduction in 2D Single-Crystal Hybrid Perovskites

Valeria Demontis, Ofelia Durante, Daniela Marongiu, Sebastiano De Stefano, Selene Matta, Angelica Simbula, Carlotta Ragazzo Capello, Giovanni Pennelli, Francesco Quochi, Michele Saba, Antonio Di Bartolomeo,* Andrea Mura, and Giovanni Bongiovanni*

Single-crystal hybrid perovskites represent an emerging class of next-generation semiconductors due to their excellent and tunable optoelectronic properties, along with a solution-based, low-temperature growth process. 2D single-crystal hybrid perovskites are especially promising as their long-range ordered multiple quantum well structure induces many peculiar properties, such as large exciton binding energy, large in-plane conductivity, and improved environmental stability, which make them suitable for low-dimensional optoelectronics applications and fundamental studies. Herein, the structural properties, morphology, and optoelectronic behavior of 2D thin film phenethylammonium lead iodide (PEA_2PbI_4) single-crystals, synthesized using the space-confined growth technique are explored. A planar device is fabricated and its spectral photoresponse is studied under broadband supercontinuum white light. Remarkably, the device exhibits an ultra-low dark current (10^{-14} A), indicative of low defect density and suppressed ion migration. Under white light, the current increases linearly with the incident power, up to a factor of 10^5, and the device achieves a specific detectivity of 10^9 Jones. The temperature and wavelength dependence of the photocurrent suggests the dissociation of excitons as one of the main mechanisms affecting photoconduction. Furthermore, stability under air exposure and illumination turns out to be remarkable.

1. Introduction

Single-crystal organic-inorganic hybrid perovskites are attracting significant interest among new-generation semiconducting materials.[1,2] Closely related to their polycrystalline counterparts, which have revolutionized photovoltaic research,[3] single crystal perovskites inherit and amplify their numerous advantages related to the tunable band gap,[4,5] high absorption coefficient, excellent photophysical properties[6–8] and low-cost solution-based synthesis.[9] Over the last 15 years, polycrystalline hybrid perovskites, especially 3D perovskites, have achieved remarkable success, particularly in photovoltaic applications. They have witnessed a significant increase in solar power conversion efficiency, rising from a few percent to over 25%.[10] Applications have extended beyond solar cells, into areas like light-emitting diodes,[11] lasers[12,13] and field effect transistors.[14] However, despite the impressive results, polycrystalline perovskites typically suffer from inherent limitations stemming from structural disorder and rapid degradation under environmental conditions. These materials exhibit a large defect density, approximately five orders of magnitude greater than single-crystal perovskites and conventional crystalline silicon.[14,15] Such defects, which include vacancies of several elements, interstitial and substitutional defects, accumulate at grain boundaries and may even cause pinholes, severely compromising both long-term material stability and device performance.[16] Defects are considered the main cause of instability of polycrystalline hybrid perovskites as they favor the penetration of humidity, oxygen and other external chemicals in the structure as well as the evaporation of volatile molecules, resulting in rapid material degradation.[17] Defects also impact the device performance, as they are a source of localized energy states acting as charge traps, providing channels for ion migration and causing relevant and often uncontrollable hysteresis effects in optoelectronic device operation.[18] In contrast, single-crystal perovskites, with their long-range spatial order and low structural defect density,[19] possess unique properties such as high charge carrier mobility, long carrier diffusion length,[20] long carrier lifetime[21] and enhanced environmental stability. In recent years, 2D and quasi-2D hybrid perovskites

V. Demontis, D. Marongiu, S. Matta, A. Simbula, F. Quochi, M. Saba, A. Mura, G. Bongiovanni
Department of Physics
University of Cagliari
S.P. Monserrato-Sestu, Monserrato 09042, Italy
E-mail: valeria.demontis@unica.it

O. Durante, S. De Stefano, A. Di Bartolomeo
Department of Physics 'E.R. Caianiello'
University of Salerno
Via Giovanni Paolo II 132, Fisciano 84084, Italy
E-mail: adibartolomeo@unisa.it

C. Ragazzo Capello, G. Pennelli
Department of Information Engineering
University of Pisa
Via Caruso 16, Pisa I-56122, Italy

The ORCID identification number(s) for the author(s) of this article can be found under https://doi.org/10.1002/adom.202402469

DOI: 10.1002/adom.202402469

have emerged as particularly promising materials for advanced optoelectronic applications. 2D hybrid perovskites are described by the general formula $A_2B_{n-1}M_nX_{3n+1}$, where A is a large-sized monovalent spacer cation, B is a small-sized monovalent organic cation or inorganic cation such as Cs^+, M is a divalent metal cation (Pb^{2+} or Sn^+), X is a halide anion, and n is the number of interconnected octahedral slabs.[22] These materials feature a distinctive structural arrangement characterized by a stack of a fixed number n of inorganic $[PbI]^6$ octahedral layers sandwiched between two large organic cations which act as spacers. For n = 1, the structure consists of single inorganic layers, usually oriented parallel to the growth substrates,[23] assembled by van der Waals interactions.[24] The multiple quantum well structure which induces strong quantum confinement effects and is responsible for a larger band gap when compared to 3D counterparts, enhanced exciton binding energy[5,25] and a very large anisotropy of the in-plane and out-of-plane electrical conductivity.[26] Variations in the number n of stacked inorganic octahedra layers and in the composition allow a broad tunability of the material band gap.[17] 2D perovskites display significantly enhanced chemical stability with respect to 3D perovskites even in their polycrystalline phase, primarily due to the large organic spacer acting as a hydrophobic protective layer against the external environment.[26,27] However, despite the chemical robustness, 2D polycrystalline hybrid perovskites display poor electronic performances, due to the inferior in-plane transport properties related to the presence of grain boundaries. The development of high-quality 2D single-crystal perovskites is thus a key focus for next-generation perovskites optoelectronic applications.[21,28] These materials, as a result of the weak van der Waals interactions between the organic layers, can also be produced in the form of nanosheets by solution-based method and mechanical exfoliation, making them a new playground for both fundamental studies and low-dimensional nano-optoelectronic applications.[29] One of the most promising applications of 2D single-crystal perovskites is photodetection. Nowadays photodetectors are employed across a wide variety of fields, ranging from medical imaging to wearable electronics, telecommunication technologies and application into optoelectronic integrated circuits.[30–32] The rising demand for performance and operation frequency requires improvement in several aspects, such as minimizing the time response, reducing the dark current and enhancing the photocurrent. In this landscape, the scientific community is actively exploring alternatives to silicon and III–V semiconductor-based technology for photodetector, including novel materials like graphene, Black Phosphorus (BP),[33] transition metal dichalcogenides (TMDs) in both 2D and 1D structures.[34–37] 2D single-crystal hybrid perovskites are also very promising materials in this field. Despite significant progress in recent years,[38] the synthesis of solution-based high-quality single-crystal perovskites is not yet a mature and well-controlled process.[39] In particular, the controlled synthesis of high-quality single crystal thin film perovskites, with thicknesses below a few micrometers, remains a significant challenge.[2,40] Most of the presented results come, in fact, from macroscale samples,[26] which cannot be easily integrated into devices. In this study, we employed space confined-growth[41] to synthesize PEA_2PbI_4 2D single crystal (SC-PEA_2PbI_4) perovskites thin films using the cooling crystallization method.[17] Here *PEA* is the acronym of phenethylammonium, $C_6H_5CH_2CH_2NH_3$. PEA was selected as the organic cation because the aromatic ring in its structure enables strong interlayer π–π stacking and enhances the structural stability and rigidity of the material.[42] The space-confined growth method, characterized by its simplicity and flexibility, facilitates the growth of high-quality single crystal thin films by creating an anisotropic growth environment that promotes horizontal growth while restricting vertical growth.[41] The materials were characterized by scanning electron microscopy (SEM), atomic force microscopy (AFM), X-ray diffraction (XRD), optical absorption and photoluminescence (PL). Subsequently, we fabricated a planar photodetector, by directly depositing silver contacts on top of the SC-PEA_2PbI_4, and studied its optoelectronic properties. The electrical characterization revealed a very low dark current and a significant increase in conductivity when exposed to light, indicating a substantial light/dark current ratio and a sharp transition from an insulating to a semiconducting state. These results suggest high crystalline quality and suppressed ion migration, which is further supported by the absence of hysteretic behavior in the photocurrent-voltage characteristics. We investigated the photoconductivity when the material is excited by a broad-band white light source and studied the photoresponse as a function of illumination intensity. To investigate the physical mechanisms governing photoinduced carrier generation, we studied the photocurrent as a function of temperature and wavelength. Remarkably, photoconductivity is significant even when illuminated with monochromatic light with energy below the band gap, resonant with the excitons absorption peak. This finding contrasts with the reported values of the exciton binding energies of 2D perovskites, which largely exceed thermal energy at room temperature and should imply an insulating behavior of optical excitations in this regime. Instead, our results suggest the presence of free charges at room temperature, providing electrical confirmation of the recent evidence, demonstrated through ultrafast spectroscopy technique, of exciton dissociation at room temperature in PEA_2PbI_4.[8] The role of excitons in governing the photocurrent is confirmed by the analysis of photocurrent temperature dependence, which unveiled an activation energy of 150 meV, consistent with the reported exciton binding energy within this material.[8,43] Importantly, the device demonstrated noteworthy stability, maintaining a constant current over a 30-h continuous exposure to air and illumination, showing only a slight current decrease after 3 days. Overall, our findings contribute to the understanding of photoconductive processes in 2D single-crystal perovskites and confirm the promising potential of such materials for advanced photodetection applications.

2. Results and Discussion

2.1. Synthesis of Single-Crystal PEA_2PbI_4

PEA_2PbI_4 is a n = 1 2D layered perovskites of the Ruddlesden–Popper (RP) family. Its structure consists of alternating single conductive layers of corner-sharing $(PbI_6)^{4-}$ octahedra sandwiched between insulating layers of phenethylammonium ($C_6H_5CH_2CH_2NH_3$, abbreviated with PEA) monovalent cations.[8] **Figure 1a** shows a pictorial representation of the material crystalline structure. PEA_2PbI_4 has a fundamental bandgap of ≈2.6 eV[44] and a high exciton binding energy of ≈200 meV.[8,43] Detailed information on the material band structure

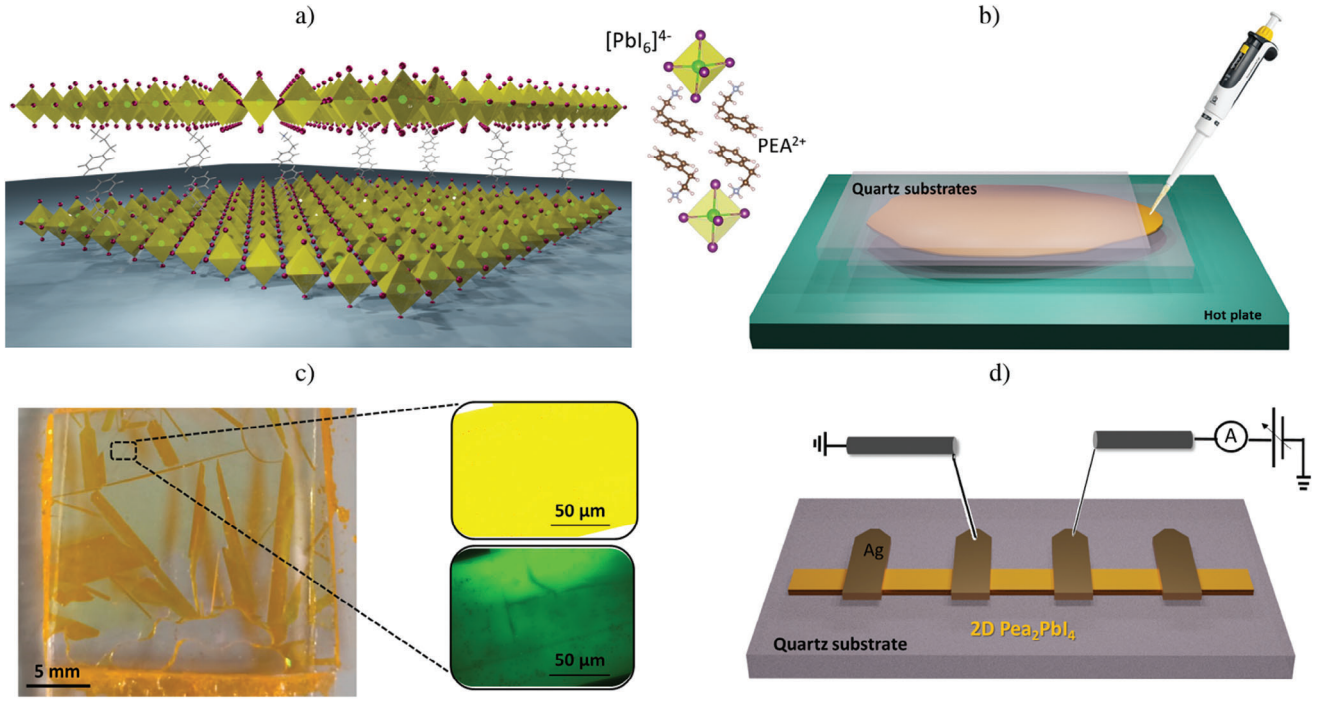

Figure 1. a) Pictorial representation of PEA_2PbI_4 crystal structure; b) Pictorial representation of the substrate stacking for the space-confined growth; c) photograph of one of the as-grown samples. The insets represent optical images at 20X magnification (top) and under UV illumination (bottom) of the crystal selected for device fabrication; d) Schematic of the device.

characterization using ultraviolet photoelectron spectroscopy can be found in Refs. [21] and [45].

A 1.8 M precursor solution of PEA_2PbI_4 in γ-butyrolactone (GBL) was solubilized in a hot plate at 80 °C under continuous stirring for 12 h. In agreement with solubility measurements presented in the literature,[21] the precursor solution is unsaturated at this temperature and exhibits a clear bright yellow color. PEA_2PbI_4 were grown by utilizing the space-confined method. Two quartz substrates were stacked slightly shifted from one another and thermalized for 5 min in the oven at a temperature of 80 °C to avoid thermal shock. 10 µL of the precursor solution was then infiltrated in the space between the substrates by capillarity, after depositing a droplet at the border of the upper substrate (Figure 1b). The temperature was then increased to 100 °C and maintained for 2 h, to ensure complete solubilization of the precursors. Then, the temperature was slowly ramped down to 20 °C at a rate of 2 °C h^{-1}. To facilitate the solvent evaporation and yield dry samples at the end of the process, dynamic vacuum conditions were applied using a scroll pump. Figure 1c shows a photograph of the as-grown sample, revealing quite large ribbon-shaped single crystals with lengths on the order of centimeters and widths varying from a few tens of µm to several hundreds of µm. After the growth, the two substrates were separated using a blade. The grown crystals were inspected by optical microscopy and under UV illumination (insets of Figure 1c). Finally, one of the grown SC-PEA_2PbI_4 single-crystal was selected for device fabrication. A planar photodetector, sketched in Figure 1d, was fabricated by directly depositing silver paste electrodes on the single crystal surface. The channel width was 115 µm and the length of the devices ranged from 300 to 400 µm.

2.2. Morphological, Structural, and Optical Characterization

Figure 2a reports the scanning electron micrograph of one of the grown crystals. The crystals display a typical ribbon shape, suggesting that during the in-plane growth, one growth direction is favored. The crystals have very sharp borders and a regular, clean and flat surface morphology, with no visible macroscopic defects. The substrate remains quite clean. The insets show two higher magnification images of one of the sample's edges (top, in which the layered structure is clearly visible) and of the surface (bottom). Figure 2b shows an AFM image on a scan area of 40 µm × 40 µm of a large crystal. A well-defined layered structure is confirmed by the thickness profile captured perpendicularly to the layer's borders (bottom right inset). In the top right inset Figure 2b), a magnification of the crystal surface was captured (15 µm × 15 µm). The image reveals an atomically flat surface, with a Root-Mean-Square (RMS) roughness of 0.4 nm.

The room temperature X-ray diffraction (XRD) pattern, shown in Figure 2c), displays a series of intense regularly-spaced diffraction peaks at 5.4°, 10.8°, 16.2°, etc. These can be indexed as the (001), (002), (003), ..., (00X) reflections in layered PEA_2PbI_4, revealing a perfect crystal orientation, with a dominant crystal growth along the [001] direction, with layers parallel to the growth substrate.[21] Figure 2d) shows the optical absorption spectrum (right axis) and the photoluminescence (PL) spectrum (left axis) under 395 nm excitation, both recorded at room temperature. Both the absorption and PL spectra are dominated by the exciton peak. The optical absorption spectrum is characterized by an evident peak, located ≈515 nm, at sub-bandgap energy. As discussed in the literature,[8,46] the presence of this peak suggests that one

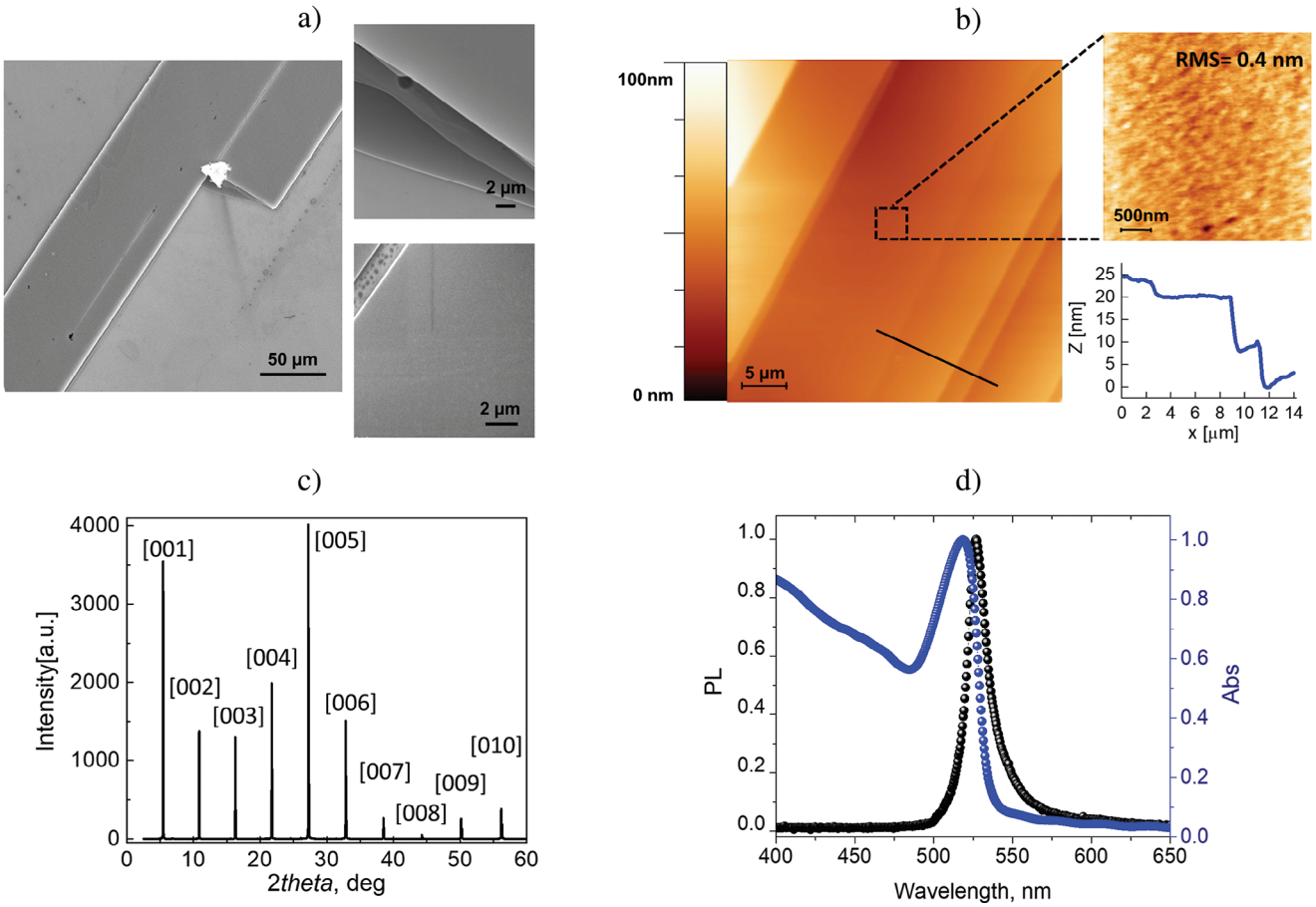

Figure 2. a) Scanning electron micrograph of as grown PEA_2PbI_4 sample. The insets show higher magnification of a detail of the sample border where the layered structure is visible and of the crystal surface; b) Atomic force microscopy image of PEA_2PbI_4. The inserts show a scan of the surface in a flat region (top right panel) and the thickness acquired along the profile marked in the main image (bottom right panel). c) XRD spectrum. d) Normalized absorption (blue) and luminescence spectrum (black).

of the most relevant mechanism of light absorption in this type of material is the generation of strongly bound excitons with large binding energies, in excess of 200 meV. The emission is also characterized by a narrow and intense photoluminescence peak, centered at ≈525 nm and with a noticeable tail at longer wavelengths. These results are a confirmation that the optoelectronic properties of PEA_2PbI_4, are strongly influenced by excitons, as the peak was attributed to the recombination of free excitons, while the tail was attributed to the recombination of localized excitons.[47]

2.3. Electrical Characterization and Photoresponse at Room Temperature

The standard electrical characterization of the PEA_2PbI_4 single crystal-based device was initially performed at room temperature using light from a white LED array with an optical power of 1.75 mW. The emission spectrum of this source ranges from 420 to 720 nm with peaks at 450 and 540 nm. The measurements were conducted at a pressure of 1.8 mbar to prevent degradation of the material by moisture and other atmospheric species. **Figure 3a**) shows the room temperature current–voltage (*I*–*V*) curves measured in dark (black curve) and under illumination (red curve). The first interesting result is the extremely low dark current, $\approx 10^{-14}$ A, sitting just above the detection limit of the experimental setup. A low conductance is expected due to the large bang gap of PEA_2PbI_4; however, the very low dark current, consistent with the best results reported in the literature and substantially below those of polycrystalline samples and other 2D materials, including TMDs,[21,48,49] provides evidence of the high quality of the material, with negligible concentrations of intragap defects states.[48] Dark current suppression is crucial for practical photodetector applications, as it is related to a high signal-to-noise ratio of the device.[50] Under illumination, the device exhibits significant room temperature photoconductivity (red curve), displaying a sharp transition from an insulating state in the dark to a semiconducting state when exposed to light. The inset of Figure 3a shows the *I*–*V* curves obtained in two- and four-probe configurations; the comparison of the two curves yields a contact resistance of 5 GΩ. The photocurrent–voltage characteristics display an ohmic behavior, and the measured light/dark current ratio exceeds 10^5, which, to the best of our knowledge, ranks among the highest reported values for perovskites-based photodetectors.[21,51] Minimizing the effect of contact resistance through 4-probe

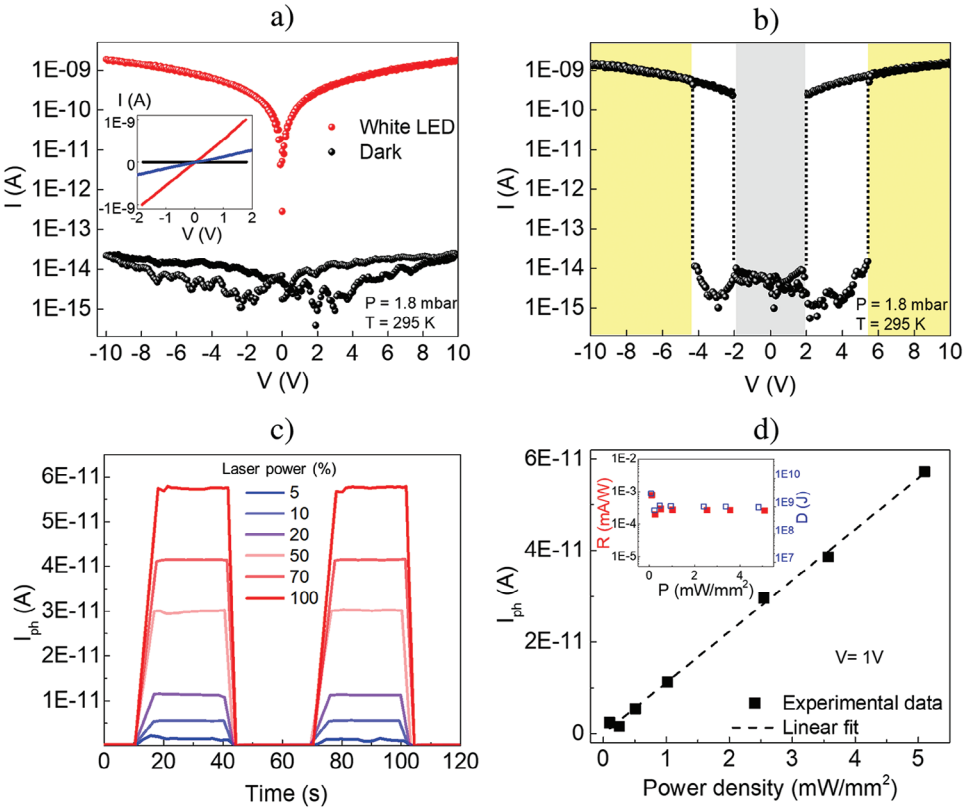

Figure 3. a) *I–V* under white LED illumination (red curve) and in dark (black curve) at T = 295 K and 1.8 mbar. Inset: *I–V* curves under LED light obtained in two- (blue) and four-probe (red) measurement configurations. b) *I–V* under white light illumination/dark cycles. c) Supercontinuum white laser excited photocurrent as a function of time at different laser powers and applied bias V = 1V. d) Photocurrent as a function of the light intensity at V = 1V. Inset: Responsivity (full red squares) and Detectivity (empty blue squares) as a function of light intensity at V = 1 V.

measurements or reducing the contact resistance through contact engineering can further enhance the photodetection performance. The study of improved contacts is currently an active area of investigation which still requires dedicated studies that go beyond the scope of this work.[52,53] The sharp transition from the insulating to the conductive state can also be observed directly by turning the light on and off during the I–V measurements, as shown in Figure 3b. The current below 10^{-14} A suddenly increases to 2×10^{-10} A at ±2 V when the light is turned on and drops again to 10^{-14} A at 6 V when the light is switched off. The symmetric behaviour indicates a similar response to illumination in both forward and reverse bias conditions. The absence of any hysteretic behavior in the current-voltage characteristics confirms the negligible effects of ion migration, even under high applied bias. Ion migration is a commonly observed phenomenon in metal halide perovskites and represents in most cases a severe drawback for practical applications.[18] Moreover, ion migration, usually favored by the presence of crystal defects, adversely affects the operational stability of perovskites-based devices and adds complexity to the understanding of fundamental aspects related to the photoexcitation and transport mechanisms in these materials.[18] Compared to standard semiconductors with rigid covalent bonding, hybrid perovskites are often characterized by a "soft" lattice structure that allows the migration of ionized defects under low activation energies, causing several undesirable effects such as high dark currents, *I–V* curve hysteresis, strong polarization effects, and other deviations from standard semiconductor behaviors. When finely controlled, ion migration can be advantageous, enabling the design of novel functionalities such as memresistive behavior for memory applications, but this level of control is still rarely achieved.[54]

We then investigated the photocurrent light intensity dependence using a white supercontinuum laser (SuperK Compact from NKT Photonics) with tunable power. This source has an emission spectrum in the 450–2400 nm, a maximum power of 110 mW, and 1 mm beam diameter. Figure 3c shows the photocurrent, extracted by subtracting the dark current from the current under illumination, at V = 1V plotted as a function of time for various laser power pulses. Due to the device high sensitivity to incident light, we started our investigation by applying a modest laser power, corresponding to 2 % of the laser maximum power. Since most of the laser power is emitted at energies below the material's bandgap, the effective incident power, calculated by integrating the laser spectrum in the material's absorption range (400–530 nm) is much lower. The effective range of variation of the laser power was 100 µW to 5 mW. The 30 s long light pulses induce a photocurrent that increases as the laser power increases, from 1.27×10^{-12} A at 100 µW to 5.74×10^{-11} A at 5 mW. As shown in Figure 3c), we observe at room temperature a noticeable, stable photocurrent, with rise and decay times below the 0.5 s sampling time of the measurement setup. A detailed analysis of the photoresponse transient behavior in 2D PEA_2PbI_4

Table 1. Responsivity and Detectivity from literature and this work.

Active layer	λ [nm]	Responsivity [A W^{-1}]	Detectivity [J]	Refs.
PEA_2PbI_4	460	98.17	1.62×10^{15}	[21]
F-PEA_2PbI_4	523	2200	2.4×10^{18}	[46]
PEA_2PbI_4 NWs	520	2.1	1.7×10^{12}	[45]
F-PEA_2PbI_4	514	1100	5×10^{17}	[56]
PA_2PbBr_4	405	2.22	2.3×10^{13}	[58]
PEA_2PbI_4	525	3.17×10^{-5}	3×10^{8}	This work

single-crystal photodetectors can be found in Ref. [21]. Remarkably, the device yields a photocurrent that increases linearly with laser power (see Figure 3d), contrasting with other perovskites-based devices.[55] Specifically, the relationship between the photocurrent (I_{ph}) and the light intensity (P) can be expressed as:

$$I_{ph} \propto P^{0.98} \tag{1}$$

The exponent close to 1 indicates an almost ideal behaviour between photoresponse and illumination intensity, confirming the ability of the device to distinguish different light intensities, even at very low laser powers.[49] The linear increase of the photocurrent with the laser power, suggests that the photogenerated current is not limited, in the explored regime, by parasitic phenomena (such as space charge effects related to unbalanced charge diffusion, non-radiative charge recombination in traps) thus favoring efficient diffusion of charges toward the electrodes. As the results of the photocurrent measurements revealed the potential of such materials for photodection applications, we calculated the figures of merit to describe the performances of the photodetectors, namely, responsivity (R) and detectivity (D).[49] Responsivity refers to the photocurrent generated per unit of incident light power on the effective photosensitive area of a photodetector:

$$R = I_{ph}/PS \tag{2}$$

where I_{ph} is the photocurrent, P the incident power density per unit area, and S denotes the effective photosensitive area, in our case 45×10^3 μm^2. Next, we calculated the detectivity, as:

$$D = \frac{R\sqrt{S}}{\sqrt{2eI_{\text{dark}}}} \tag{3}$$

where e is the elementary charge and I_{dark} represents the dark current. I_{dark} is at the detection limit of our experimental setup and is independent of light frequency. We note that, according to Ref. [21], in 2D PEA_2PbI_4 single crystal grown using the space-confined approach, the noise current is primarily shot noise, also independent of frequency. Responsivity and Detectivity, extracted at an applied voltage of V = 1 V, are reported in the inset of Figure 3d. As expected, the values of R and D for the PEA_2PbI_4 single crystal device (Figure 3e) exhibit an almost constant behavior in the explored light intensity range, but are significantly below other reported values,[21,46,56] likely due to the non-optimal electric contact between the silver leads and the material, which requires a dedicated analysis. **Table 1** presents a comparison of the results from this work with the highest-performing photodetectors that utilize 2D perovskites. Our results, featuring extremely low dark current, linear behavior and reasonable responsivity in a broad power range, suggest the potential of SC-PEA_2PbI_4 for integration into devices that require constant operation under a variety of illumination conditions.[57]

2.4. Photoresponse Dependence on Temperature and Wavelength

To further investigate the physical mechanisms governing photoconduction in SC-PEA_2PbI_4, we studied the photocurrent as a function of temperature and wavelength. We first investigated the photocurrent at different temperatures in the range of 100–400 K using white LED illumination (**Figure 4a**). To the best of our knowledge, no phase transitions occur in this temperature range. The photocurrent is almost constant below 200 K and then clearly increases when the temperature rises above 200 K. Figure 4b shows that the temperature dependence of the current in the 200–400 K range is well-fitted by the Arrhenius equation:

$$I_{ph} = I_0 e^{-\frac{E_A}{k_B T}} \tag{4}$$

where k_B is the Boltzmann constant, T is the temperature, E_A is the activation energy. The extracted value of the activation energy is 150 meV. The results suggest that, with the increasing temperature, the thermal energy enables the dissociation of excitons, generating free charges which can contribute to the photocurrent. This points to a relevant role of exciton dynamics in governing photocurrent generation in PEA_2PbI_4.

We also studied the photocurrent as a function of wavelength at room temperature. Figure 4c,d shows the photocurrent and responsivity as a function of wavelength. Interestingly, the photocurrent and the responsivity curves, in addition to a broader band at energies above the fundamental bandgap, related to interband transitions, present a distinct peak at 526±3 nm, corresponding to the absorption peak. This result implies that when the material is resonantly excited at the exciton energy and cold excitons are injected into the material, a free-carrier population is spontaneously generated. This finding contrasts with the widely accepted understanding that excitons in PEA_2PbI_4 and other 2D perovskites are strongly bound, with binding energies (≈200 meV) which largely exceed thermal energy at room temperature. Instead, the results suggest that a fraction of the generated excitons dissociates at much lower energy. This finding supports recent studies which have also reported evidence of exciton dissociation at room temperature, obtained using time-resolved spectroscopic techniques, the physical origin of which is still under discussion.[8,56] In panel (c), the photocurrent at 450 nm is relatively low because the exciting light is characterized by low intensity in that spectral region. Our work provides a confirmation of this phenomenon using electrical probing and further evidence of the exceptional optoelectronic properties of this material.

2.5. Stability in Air

The environmental stability of the material was investigated by monitoring the photocurrent at atmospheric pressure for

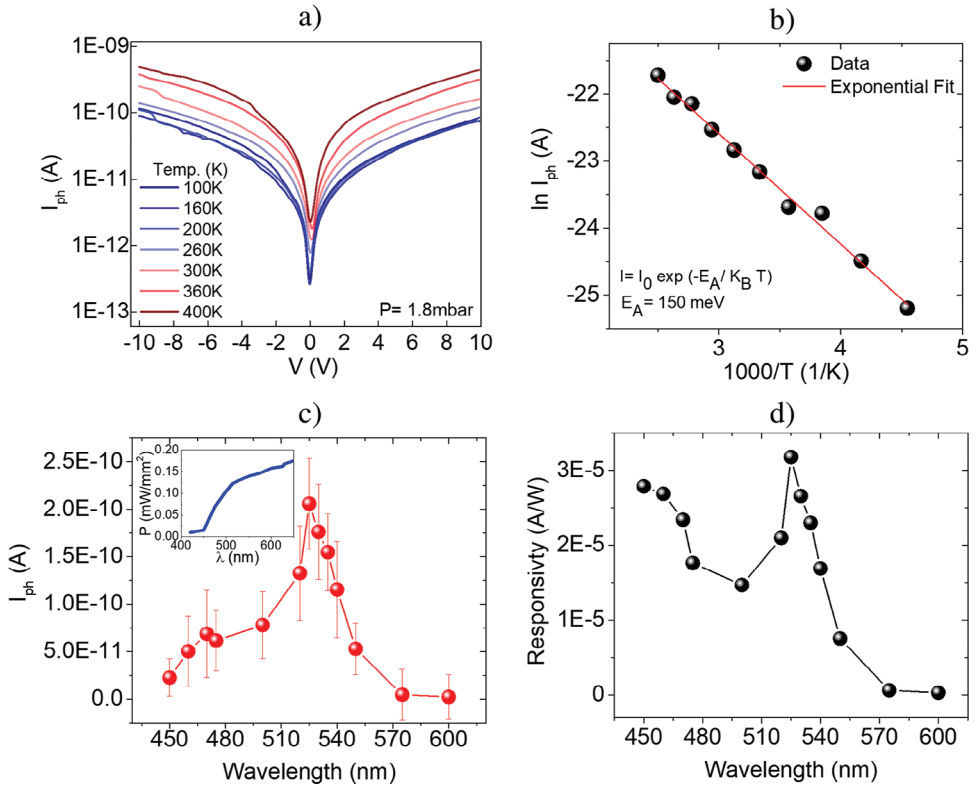

Figure 4. a) *I–V* at different temperatures under white LED illumination at 1.8 mbar. b) Photocurrent versus 1000/T plot and Arrhenius equation fit. c) Photocurrent as a function of wavelength at room temperature and ambient pressure. Inset: laser power density spectrum. d) Responsivity as a function of wavelength.

≈3 days. **Figure** 5a presents the *I–V* characteristics and Figure 5b the photocurrent over time for the PEA_2PbI_4 single crystal-based device exposed to ambient air conditions without any protective layer. Rapid degradation in environmental conditions is the most severe drawback of halide perovskites. Several strategies have been adopted to preserve the electrical and structural stability of the material, such as surface passivation, interface engineering, and device encapsulation, which have been shown to be effective in reducing defects in perovskite films, as well as the incorporation of certain materials can lead to improved surface morphology, which in turn reduces unwanted recombination of charge carriers.[59,60] One of the expected advantages of 2D single-crystal perovskites is enhanced stability. Figure 5a,b shows that the device exhibits negligible electrical degradation over a time of ≈30 h under continuous exposure to air and LED illumination. As displayed in panel (5b), a drop in current, from 3.5×10^{-10}A to 4.36×10^{-11} A, occurs after ≈3 days. These results confirm the good stability of SC-PEA_2PbI_4.

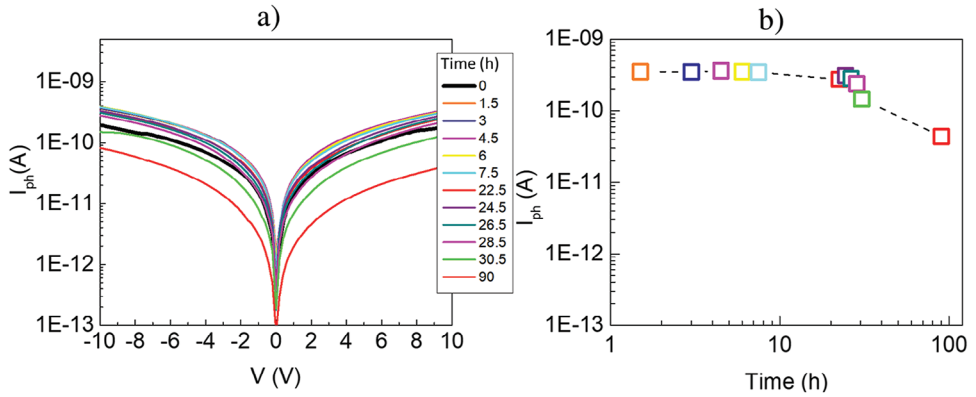

Figure 5. a) *I–V* characteristics at different times at room temperature and ambient pressure and b) photocurrent versus time under continuous LED illumination and storage in air.

3. Conclusion

In this study we demonstrated the growth of high-quality 2D layered single-crystals of (PEA_2PbI_4) perovskites, using a low-cost, solution-based process. Single-crystals with thickness below 5 µm and lateral areas up to 5 mm^2 were grown using the space confined approach. We investigated the optoelectronic properties of 2D PEA_2PbI_4 single-crystal perovskite planar devices, contributing to the understanding of the mechanisms behind photoconductivity of this material and assessing its notable capabilities in the context of photodetection applications. Among the most significant results, we observed an extremely low dark current (10^{-14} A), attributed to a high crystalline quality and suppressed ion migration, confirmed by the absence of hysteretic behaviors in the *I–V* characteristics under illumination. Moreover, the material displayed significant increase in conductivity under illumination, with linear dependence on the incident power and a maximum light/dark current ratio of the order 10^5, along with a high specific detectivity (10^9 Jones). The analysis of the photocurrent dependence on temperature and wavelength revealed the strong contribution of excitons to photoconduction mechanisms at room temperature, supporting recent findings of spontaneous exciton dissociation at room temperature in PEA_2PbI_4. This mechanism extends the photoresponse range of the material below the fundamental bandgap. Furthermore, the device displayed notable stability, with unaltered performances over a time of 30 h after continuous direct exposure to air and illumination. Our findings contribute to the understanding of photoconductive processes in 2D single-crystal perovskites and confirm the potential of these materials as promising candidates for advanced photodetection applications.

4. Experimental Section

Single-Crystals of PEA_2PbI_4 were synthesized by the space-confined growth technique. A precursor solution of PEA_2PbI_4 1.8 M in γ-butyrolactone (GBL) was prepared by dissolving lead iodide (PbI_2) (from Sigma Aldrich) and phenethylammonium iodide (PEAI) (from Greatcell-solar) in a 1:2 molar ratio and maintaining the mixture in a hot plate at 80 °C under continuous stirring for 12 h. Before use, the solution was filtered using a nylon filter with a pore size of 40 µm. Prior to growth, quartz substrates measuring 1.5 cm × 1.5 cm were cleaned via sonication in acetone followed by rinsing in isopropyl alcohol. Two quartz substrates were stacked slightly shifted from one another and thermalized for 5 min in the oven at a temperature of 80 °C. A micropipette with a pre-thermalized tip was used to pick up 10 µL of the precursor solution, which was then infiltrated between the substrates by capillarity. The temperature was first increased to 100 °C and maintained for 2 h, after which it was slowly ramped down to 20 °C at a rate of 2 °C h^{-1}. To facilitate solvent evaporation and yield dry samples at the end of the process, dynamic vacuum conditions were applied using a scroll pump. The substrates were then separated using a blade for further characterization and device fabrication The surface topography and film roughness were measured by atomic force microscopy (AFM) using a NT-MDT Solver P47H-Pro instrument in semi-contact mode. Images were analyzed using WSxM software.[61] The X-ray diffraction patterns were acquired using a Bruker D8 Advance diffractometer equipped with Cu Kα radiation (λ = 1.5406 Å). UV–VIS optical absorption was measured using a Jasco V-770 spectrofotometer, while the static photoluminescence was acquired using a Photon Control Spectrometer-SPM-002 under 395 nm excitation. Metal contacts were made using a DUpont 4929N conductive silver paste. The electric measurements were conducted in a cryogenic Janis ST-500 Probe Station using a Keithley 4200 semiconductor analyzer. Photocurrent measurements were performed under the illumination by a supercontinuum white laser (SuperK COMPACT by NKT Photonics) with a maximum power of 110 mW, wavelength in the range 450–2400 nm, and 1 mm beam diameter. Wavelength-dependent measurement were performed using a monochromator (Sciencetech Inc.) with 20 nm bandwidth.

Acknowledgements

V.D. and O.D. contributed equally to this work. V.D. acknowledges the support of the Project "Network 4 Energy Sustainable Transition–NEST," Spoke 1, Project code PE0000021, funded under the National Recovery and Resilience Plan (PNRR), Mission 4, Component 2, Investment 1.3– Call for tender No. 1561 of 11.10.2022 of Ministero dell'Università e della Ricerca (MUR); funded by the European Union-NextGenerationEU. A.D.B. and O.D. acknowledge the financial support from the University of Salerno, with grant ORSA223384 and ORSA235199. G.B., A.M., and D.M. acknowledge the support of Italian Ministry for University and Research (MUR), PRIN 2022 grant P20224PJJN. G.B. acknowledges the support of the Italian Ministry for University and Research (MUR), PRIN 2022 grant 2022XP37C7. D.M., G.B., M.S., and A.M. acknowledge the support of Fondazione di Sardegna, grant F73C22001160007.

Open access publishing facilitated by Universita degli Studi di Cagliari, as part of the Wiley - CRUI-CARE agreement.

Conflict of Interest

The authors declare no conflict of interest.

Data Availability Statement

The data that support the findings of this study are available from the corresponding author upon reasonable request.

Keywords

2D single-crystal hybrid perovskites, advanced optoelectronic materials, exciton dynamics, photoconduction

Received: September 11, 2024
Revised: November 6, 2024
Published online:

[1] C. Li, H. Sun, S. Gan, D. Dou, L. Li, *Mater. Futures.* **2023**, *2*, 042101.
[2] B. Murali, H. K. Kolli, J. Yin, R. Ketavath, O. M. Bakr, O. F. Mohammed, *ACS Mater. Lett.* **2020**, *2*, 184.
[3] *Nat Energy* **2019**, *4*, 1.
[4] J. H. Noh, S. H. Im, J. H. Heo, T. N. Mandal, S. I. Seok, *Nano Lett.* **2013**, *13*, 17649.
[5] A. A. Zhumekenov, M. I. Saidaminov, M. A. Haque, E. Alarousu, S. P. Sarmah, B. Murali, I. Dursun, X.-H. Miao, A. L. Abdelhady, T. Wu, O. F. Mohammed, O. M. Bakr, *ACS Energy Lett.* **2016**, *1*, 32.
[6] A. Simbula, R. Pau, Q. Wang, F. Liu, V. Sarritzu, S. Lai, M. Lodde, F. Mattana, G. Mula, A. Geddo Lehmann, I. D. Spanopoulos, M. G. Kanatzidis, D. Marongiu, F. Quochi, M. Saba, A. Mura, G. Bongiovanni, *Adv. Opt. Mater.* **2021**, *9*, 2100295.
[7] S. D. Stranks, G. E. Eperon, G. Grancini, C. Menelaou, M. J. P. Alcocer, T. Leijtens, L. M. Herz, A. Petrozza, H. J. Snaith, *Science* **2013**, *342*, 341.
[8] A. Simbula, L. Wu, F. Pitzalis, R. Pau, S. Lai, F. Liu, S. Matta, D. Marongiu, F. Quochi, M. Saba, A. Mura, G. Bongiovanni, *Nat. Commun.* **2023**, *14*, 4125.

[9] L. Dou, Y. Yang, J. You, Z. Hong, W.-H. Chang, G. Li, Y. Yang, *Nat. Commun.* **2014**, *5*, 1.
[10] H. Su, Z. Xu, X. He, Y. Yao, X. Zheng, Y. She, Y. Zhu, J. Zhang, S. F. Liu, *Adv. Mater.* **2024**, *36*, 2306724.
[11] D. Yang, B. Zhao, T. Yang, R. Lai, D. Lan, R. H. Friend, D. Di, *Adv. Funct. Mater.* **2021**, *32*, 9.
[12] F. Zhao, A. Ren, P. Li, Y. Li, J. Wu, Z. M. Wang, *ACS Nano* **2022**, *16*, 7116.
[13] A. Liu, G. Guan, X. Chai, N. Feng, M. Lu, X. Bai, Y. Zhang, *Laser Photonics Rev.* **2022**, *16*, 10.
[14] A. Liu, H. Zhu, S. Bai, Y. Reo, M. Caironi, A. Petrozza, L. Dou, Y.-Y. Noh, *Nat. Electron.* **2023**, *6*, 559.
[15] D. Shi, V. Adinolfi, R. Comin, M. Yuan, E. Alarousu, A. Buin, Y. Chen, S. Hoogland, A. Rothenberger, K. Katsiev, Y. Losovyj, X. Zhang, P. A. Dowben, O. F. Mohammed, E. H. Sargent, O. M. Bakr, *Science* **2015**, *347*, 519.
[16] Y. Chen, H. Zhou, *J. Appl. Phys.* **2020**, *128*, 6.
[17] Z. Zhang, W. Kim, M. J. Ko, Y. Li, *Nano Converg.* **2023**, *10*, 1.
[18] T. Zhang, H. Chen, Y. Bai, S. Xiao, L. Zhu, C. Hu, Q. Xue, S. Yang, *Nano Energy* **2016**, *26*, 620.
[19] Z. Xiao, Y. Yan, *Adv. Energy Mater.* **2017**, *7*, 22.
[20] Q. Dong, Y. Fang, Y. Shao, P. Mulligan, J. Qiu, L. Cao, J. Huang, *Science* **2015**, *347*, 967.
[21] Y. Liu, Y. Zhang, Z. Yang, H. Ye, J. Feng, Z. Xu, X. Zhang, R. Munir, J. Liu, P. Zuo, Q. Li, M. Hu, L. Meng, K. Wang, D.-M. Smilgies, G. Zhao, H. Xu, Z. Yang, A. Amassian, J. Li, K. Zhao, S. Liu, *Nat. Commun.* **2018**, *9*, 1.
[22] T. L. Leung, I. Ahmad, A. A. Syed, A. M. C. Ng, J. Popović, A. B. Djurišić, *Commun. Mater.* **2022**, *3*, 63.
[23] Y. Zhang, R. Wang, Z. Tan, *J. Mater. Chem. A* **2023**, *11*, 11607.
[24] J. Duan, H. Cen, J. Dai, Z. Wu, J. Xi, *Mater. Today Electron.* **2024**, *8*, 100097.
[25] C. C. Stoumpos, D. H. Cao, D. J. Clark, J. Young, J. M. Rondinelli, J. I. Jang, J. T. Hupp, M. G. Kanatzidis, *Chem. Mat.* **2016**, *28*, 2852.
[26] K. Wang, C. Wu, D. Yang, Y. Jiang, S. Priya, *ACS Nano* **2018**, *12*, 4919.
[27] S.-Q. Luo, J.-F. Wang, B. Yang, Y.-B. Yuan, *Front. Phys.* **2019**, *14*, 5.
[28] N. Wang, L. Cheng, R. Ge, S. Zhang, Y. Miao, W. Zou, C. Yi, Y. Sun, Y. Cao, R. Yang, Y. Wei, Q. Guo, Y. Ke, M. Yu, Y. Jin, Y. Liu, Q. Ding, D. Di, L. Yang, G. Xing, H. Tian, C. Jin, F. Gao, R. H. Friend, J. Wang, W. Huang, *Nat. Photonics* **2016**, *10*, 699.
[29] B. Cheng, T.-Y. Li, P. Maity, P.-C. Wei, D. Nordlund, K.-T. Ho, D.-H. Lien, C.-H. Lin, R.-Z. Liang, X. Miao, I. A. Ajia, J. Yin, D. Sokaras, A. Javey, I. S. Roqan, O. F. Mohammed, J.-H. He, *Commun. Phys.* **2018**, *1*, 1.
[30] S. Cai, X. Xu, W. Yang, J. Chen, X. Fang, *Adv. Mater.* **2019**, *31*, 18.
[31] Z. Ma, Y. Zhang, T. Li, X. Tang, H. Zhao, J. Li, C. Ma, J. Yao, *Appl. Phys. A* **2020**, *126*, 11.
[32] Y. Hao, S. Xiang, G. Han, J. Zhang, X. Ma, Z. Zhu, X. Guo, Y. Zhang, Y. Han, Z. Song, Y. Liu, L. Yang, H. Zhou, J. Shi, W. Zhang, M. Xu, W. Zhao, B. Pan, Y. Huang, Q. Liu, Y. Cai, J. Zhu, X. Ou, T. You, H. Wu, B. Gao, Z. Zhang, G. Guo, Y. Chen, Y. Liu, et al., *Sci China Inf Sci* **2021**, *64*, 10.
[33] A. Kumar, L. Viscardi, E. Faella, F. Giubileo, K. Intonti, A. Pelella, S. Sleziona, O. Kharsah, M. Schleberger, A. Di Bartolomeo, *Nano Express* **2023**, *4*, 014001.
[34] F. Xia, T. Mueller, Y.-m. Lin, A. Valdes-Garcia, P. Avouris, *Nat. Nanotechnol.* **2009**, *4*, 839.
[35] A. Pelella, K. Intonti, O. Durante, A. Kumar, L. Viscardi, S. De Stefano, P. Romano, F. Giubileo, H. Neill, V. Patil, L. Ansari, B. Roycroft, P. K. Hurley, F. Gity, A. Di Bartolomeo, *Discover Nano* **2024**, *19*, 1.
[36] O. Durante, S. D. Stefano, D. Capista, M. Passacantando, A. Zak, F. Giubileo, L. Camilli, A. D. B. Sr, In *IEEE Nanotechnology Materials and Devices Conf. (NMDC)*, IEEE, New York **2023**, 676.
[37] A. Di Bartolomeo, A. Kumar, O. Durante, A. Sessa, E. Faella, L. Viscardi, K. Intonti, F. Giubileo, N. Martucciello, P. Romano, S. Sleziona, M. Schleberger, *Mater. Today Nano* **2023**, *24*, 100382.
[38] J. Li, J. Wang, J. Ma, H. Shen, L. Li, X. Duan, D. Li, *Nano Converg.* **2019**, *10*, 1.
[39] A. Simbula, V. Demontis, F. Quochi, G. Bongiovanni, D. Marongiu, *ACS Omega* **2024**, *9*, 36865.
[40] Y.-H. Deng, Z.-Q. Yang, R.-M. Ma, *Nano Converg.* **2020**, *7*, 1.
[41] L. Li, J. Liu, M. Zeng, L. Fu, *Nano Research* **2020**, *14*, 1609.
[42] S. Sui, J. Zhou, A. Wang, G. Hu, W. Meng, C. Wang, Y. Liu, J. Wu, Z. Deng, *Nanoscale Adv.* **2021**, *3*, 3875.
[43] X. Gao, X. Zhang, W. Yin, H. Wang, Y. Hu, Q. Zhang, Z. Shi, V. L. Colvin, W. W. Yu, Y. Zhang, *Adv. Sci.* **2019**, *6*, 22.
[44] D. Shin, F. Zu, E. R. Nandayapa, L. Frohloff, E. Albert, E. J. W. List-Kratochvil, N. Koch, *Adv. Funct. Mater.* **2022**, *33*, 2.
[45] T. Gao, Y. Jiang, S. Yang, J. Hu, Z. Zhang, P. Tang, Y. Cui, M. Sulaman, L. Tang, B. Zou, *J. Alloys Compd.* **2023**, *940*, 168894.
[46] K. J. Riisnaes, M. Alshehri, I. Leontis, R. Mastria, H. T. Lam, L. De Marco, A. Coriolano, M. F. Craciun, S. Russo, *ACS Appl. Mater. Interfaces* **2024**, *16*, 31399.
[47] W. Li, S. Yang, B. Guo, X. Fu, X. Zeng, C. Yan, J. Cao, Q. Wang, W. Yang, *J. Alloys Compd.* **2023**, *936*, 168312.
[48] W. Peng, J. Yin, K.-T. Ho, O. Ouellette, M. De Bastiani, B. Murali, O. El Tall, C. Shen, X. Miao, J. Pan, E. Alarousu, J.-H. He, B. S. Ooi, O. F. Mohammed, E. Sargent, O. M. Bakr, *Nano Lett.* **2017**, *17*, 4759.
[49] Y. Tu, Y. Xu, J. Li, Q. Hao, X. Liu, D. Qi, C. Bao, T. He, F. Gao, W. Zhang, *Small* **2020**, *16*, 52.
[50] Y. Fang, J. Huang, *Adv. Mater.* **2015**, *27*, 2804.
[51] H. Wang, Y. Chen, D. Li, *J. Extrem. Manuf.* **2023**, *5*, 012004.
[52] F. Li, W. Yu, X. Guan, T. Wu, *Acc. Mater. Res.* **2021**, *3*, 8.
[53] Y. Wang, Z. Wan, Q. Qian, Y. Liu, Z. Kang, Z. Fan, P. Wang, Y. Wang, C. Li, C. Jia, Z. Lin, J. Guo, I. Shakir, M. Goorsky, X. Duan, Y. Zhang, Y. Huang, X. Duan, *Nat. Nanotechnol.* **2020**, *15*, 768.
[54] K. Sakhatskyi, R. A. John, A. Guerrero, S. Tsarev, S. Sabisch, T. Das, G. J. Matt, S. Yakunin, I. Cherniukh, M. Kotyrba, Y. Berezovska, M. I. Bodnarchuk, S. Chakraborty, J. Bisquert, M. V. Kovalenko, *ACS Energy Lett.* **2022**, *7*, 3401.
[55] Y. Xue, J. Yuan, J. Liu, S. Li, *Nanomater.* **2018**, *8*, 591.
[56] R. Mastria, K. J. Riisnaes, A. Bacon, I. Leontis, H. T. Lam, M. A. S. Alshehri, D. Colridge, T. H. E. Chan, A. De Sanctis, L. De Marco, L. Polimeno, A. Coriolano, A. Moliterni, V. Olieric, C. Giannini, S. Hepplestone, M. F. Craciun, S. Russo, *Adv. Funct. Mater.* **2024**, *34*, 2401903.
[57] Y. Zhang, Y. Liu, Z. Xu, H. Ye, Q. Li, M. Hu, Z. Yang, S. F. Liu, *J. Mater. Chem. C* **2019**, *7*, 1584.
[58] K. Dong, H. Zhou, Z. Gao, M. Xu, L. Zhang, S. Zhou, H. Cui, S. Wang, C. Tao, W. Ke, F. Yao, G. Fang, *Adv. Funct. Mater.* **2023**, *34*, 1.
[59] A. A. Khan, N. Kumar, U. Jung, W. Heo, Z. Tan, J. Park, *Nanoscale Horiz.* **2023**, *8*, 1577.
[60] F. Corsini, G. Griffini, *J.Phys. Energy* **2020**, *2*, 031002.
[61] I. Horcas, R. Fernández, J. M. Gómez-Rodríguez, J. Colchero, J. Gómez-Herrero, A. M. Baro, *Rev. Sci. Instrum.* **2007**, *78*, 1.